

# High-Efficiency Digital Inkjet-Printed Non-Fullerene Polymer Blends Using Non-Halogenated Solvents

Pavlo Perkhun, Wolfgang Köntges, Florent Pourcin, Daniel Esteouille, Elena Barulina, Noriyuki Yoshimoto, Pascal Pierron, Olivier Margeat, Christine Videlot-Ackermann, Anil Kumar Bharwal, David Duché, Carmen Ruiz Herrero, Cedric Gonzales, Antonio Guerrero, Juan Bisquert, Rasmus R. Schröder, Martin Pfannmöller,\* Sadok Ben Dkhil,\* Jean-Jacques Simon, and Jörg Ackermann\*

Inkjet printing (IJP) of polymer solar cells is ideal for small-area off-grid electronics with low power consumption. However, IJP is quite a complex technique compared with techniques such as spin coating or doctor blading. The IJP of polymer blends is reported based on ITIC derivatives as non-fullerene acceptors (NFAs) using non-halogenated solvents. The results show that fluorination of NFA is essential to form highly stable inks in *o*-xylene, because ITIC has significantly insufficient solubility compared with ITIC-4F. The importance of tetralin as a multifunctional co-solvent for printing highly efficient PM6:ITIC-4F blends is demonstrated, as even at very low concentrations, tetralin not only improves ink jetability and open nozzle time, but also improves drying behavior of the blend layer, resulting in blends with homogeneous micro- and nanoscale morphology. The resulting solar cells using inkjet-printed polymer blends show a maximum efficiency of 10.1%. Moreover, IJP produces significant changes in the nanoscale and microscale morphology. In particular, the formation of a thin PM6 capping layer on the blend surface along with improved phase separation and crystallinity in both the donor and acceptor greatly reduces the recombination of charge carriers in thick blends, making inkjet-printed photoactive films very promising for industrial applications.

## 1. Introduction

Over the last decade, the development of non-fullerene acceptor (NFA) resulted in power conversion efficiencies (PCEs) of organic solar cells (OSCs) exceeding 17%.<sup>[1,2]</sup> This advances OSCs closer to commercial applications such as powering the off-grid electronics including the Internet of Things (IoT).<sup>[3]</sup> To date, the high-efficiency solar cells based on NFA materials are typically manufactured by spin coating (SC) with halogenated solvents.<sup>[1,2,4,5]</sup> Hence, to scale up the technology toward industrial processing, typography methods such as screen printing,<sup>[6]</sup> slot-die coating,<sup>[7,8]</sup> and digital printing<sup>[9,10]</sup> together with the use of non-halogenated solvents for the blend ink formulation have to be implemented for NFAs as anticipated

P. Perkhun, E. Barulina, Dr. O. Margeat, Dr. C. Videlot-Ackermann, Dr. J. Ackermann  
Aix Marseille University  
CINAM - Centre Interdisciplinaire de Nanoscience de Marseille  
UMR CNRS 7325  
13288 Marseille, France  
E-mail: jorg.ackermann@univ-amu.fr

W. Köntges, Dr. M. Pfannmöller  
CAM – Centre for Advanced Materials  
Heidelberg University  
69120 Heidelberg, Germany  
E-mail: m.pfannmoeller@uni-heidelberg.de


Dr. F. Pourcin, D. Esteouille, P. Pierron, Dr. S. Ben Dkhil  
Dracula Technologies  
3 Rue Georges Auric, Valence 26000, France  
E-mail: s.bendkhil@dracula-technologies.com

Prof. N. Yoshimoto  
Department of Physical Science and Materials Engineering  
Iwate University  
Ueda Morioka 020 8551, Japan

Dr. A. K. Bharwal, Dr. D. Duché, Dr. C. R. Herrero, Prof. J.-J. Simon  
Aix Marseille University  
Université de Toulon  
IM2NP - Institut Matériaux Microélectronique Nanosciences de Provence  
UMR CNRS 7334  
Marseille IM2NP, France

C. Gonzales, Prof. A. Guerrero, Prof. J. Bisquert  
Institute of Advanced Materials (INAM)  
Universitat Jaume I  
Castelló 12006, Spain

Prof. R. R. Schröder  
3DMM2O – Cluster of Excellence (EXC-2082/1 – 390761711) and CAM –  
Centre for Advanced Materials  
Heidelberg University  
69120 Heidelberg, Germany

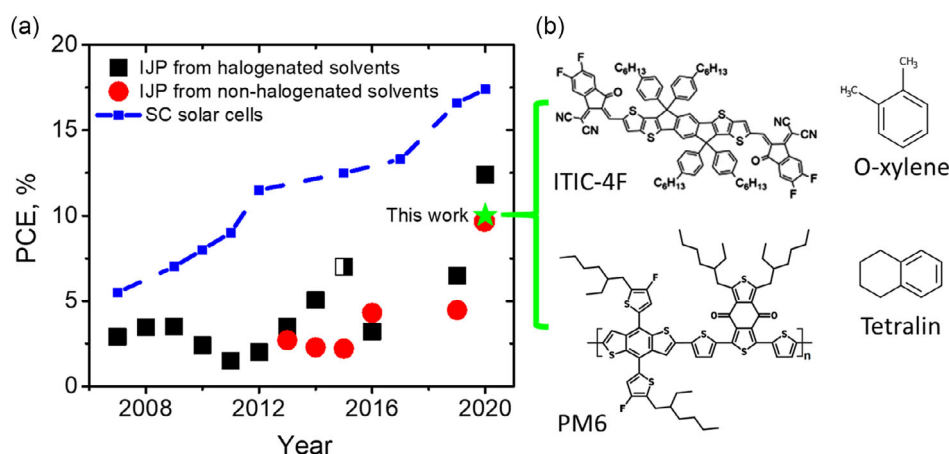
 The ORCID identification number(s) for the author(s) of this article can be found under <https://doi.org/10.1002/aesr.202000086>.

© 2021 The Authors. Advanced Energy and Sustainability Research published by Wiley-VCH GmbH. This is an open access article under the terms of the Creative Commons Attribution License, which permits use, distribution and reproduction in any medium, provided the original work is properly cited.

DOI: 10.1002/aesr.202000086

before for fullerene-based OSCs.<sup>[11,12]</sup> Among those deposition techniques, inkjet printing (IJP) is outstanding as it is a contactless deposition technique<sup>[13,14]</sup> that provides digital freedom of layer design on various substrates with low material usage.<sup>[10,14,15]</sup> It has been successfully applied for manufacturing of OSCs, whereas printing of the photoactive layers as well as the interfacial layers and electrodes<sup>[9,10,16–19]</sup> has been demonstrated. However, the PCE of inkjet-printed OSCs is still much lower compared with the high efficiency reported recently for NFA-based solar cells using deposition techniques such as SC or doctor blading, as shown in **Figure 1a**. Moreover, the replacement of highly toxic solvents such as chlorobenzene in IJP of polymer solar cells remains a crucial challenge due to the difficulties of morphological control within the photoactive layer upon the system solvent changes.<sup>[20]</sup> Indeed, inkjet-printed solar cells using more industrial-relevant non-halogenated solvents that have lower effects on health and environment show performances that are generally reduced compared with optimized devices.<sup>[10,12,21]</sup> In particular, IJP of NFA-based photoactive layers using non-halogenated solvent mixture based on *o*-xylene and tetralin resulted in solar cells with the low PCEs of 4.46%<sup>[22]</sup> compared with 6.67% obtained for halogenated solvents.<sup>[22,23]</sup> The performance losses may be addressed to the low solubility of the NFA in *o*-xylene inducing poor blend morphology. To further boost the performance of solar cells processed by IJP using non-halogenated solvent to higher level, it is now essential to understand more, in detail, the impact of IJP on the layer formation and nanoscale morphology of blend compared with SC and to improve blend morphology by selecting suitable NFA materials and non-chlorinated solvent mixture combinations. In general, layer formation and drying kinetics of inkjet-printed photoactive layers are fundamentally different from SC processes impeding the nanoscale phase separation of the blend.<sup>[24]</sup> First, the blend materials have to form stable suspensions with high resistance toward chemical or physical changes over time, allowing to enhance the open nozzle time<sup>[15]</sup> (ONT), which is the time a printing nozzle can stay uncovered and idle during printing before getting clogged. Furthermore, fine control over the nanoscale phase separation inside the blend using IJP is governed by

the solubility of both donor and acceptor materials in the solvent of the ink. These requirements, thus, demand stable and highly soluble donor and acceptor materials. The ejection of the ink from the print head requires suitable viscosity, surface tension, and vapor pressure to form satellite-free droplets of controlled volume.<sup>[25]</sup> Furthermore, the drying speed of the printed layers<sup>[26,27]</sup> has to be optimized, for which a solvent mixture comprising of *o*-xylene, indane, and tetralin was found to be a good strategy.<sup>[10,12,21]</sup> Those parameters can be considered as rather blend material-independent. In this work, we present a detailed study on optimization of IJP of high-efficiency non-fullerene blends from non-halogenated solvent mixture and compare the optimal layer morphology and corresponding device performances with those obtained by SC. Most scientific works on IJP use lab-scale inkjet printer with small numbers of nozzles corresponding to printing processes that are rather far away from industrial standards. Therefore, we selected here the printing of the photoactive layer with a semi-industrial digital printer with print head containing 512 nozzles that are compatible with industrial large scale printing. As high-efficiency NFA material, we selected polymer blends based on poly[(2,6-(4,8-bis(5-(2-ethylhexyl)thiophen-2-yl)benzo[1,2-b:4,5-b']dithiophene)-co-(1,3-di(5-thiophene-2-yl)-5,7-bis(2-ethylhexyl)benzo[1,2-c:4,5-c']dithiophene-4,8-dione)] known as PBDB-T<sup>[28]</sup> and 3,9-bis(2-methylene-(3-(1,1-dicyanomethylene)-indanone)-5,5,11,11-tetrakis(4-hexylphenyl)-dithieno[2,3-d':3'-d']-s-indaceno[1,2-b:5,6-b']dithiophene known as ITIC,<sup>[29]</sup> and its fluorinated derivatives PM6<sup>[30]</sup> and ITIC-4F,<sup>[31]</sup> respectively. Indeed, ITIC-4F has shown high compatibility with non-halogenated solvents such as *o*-xylene.<sup>[32]</sup> To adjust the printing parameters, inks based on pure *o*-xylene and *o*-xylene–tetralin solvent mixture were studied as demonstrated by Baran and co-workers.<sup>[22]</sup> Our results reveal that layer formation and nanoscale morphology of inkjet-printed blends depend strongly on the chemical structure of the NFA and, more importantly, on the solvent additives that allow to improve jetting and drying properties of the blend layers. Indeed, we show that fluorination of the NFA is essential to form highly stable inks in *o*-xylene as ITIC shows clearly insufficient solubility compared with ITIC-4F. Although



**Figure 1.** a) The evolution of the PCE over time for the OSCs made by SC and IJP from different solvents. Half-filled squares represent data obtained from commercial ink. For the references of the data points, see Table S1, Supporting Information. b) Chemical structures of the NFA ITIC-4F, the donor polymer PM6, and the solvents used for the ink formulation.

PM6:ITIC-4F blends are highly soluble in o-xylene, it still leads to poor printing and film drying behavior that overall leads to strong performance losses in solar cells compared with reference devices using spin-coated photoactive layers. Importantly, our results reveal that tetralin is a multifunctional co-solvent that is essential for the printing of high-efficient solar cells. Indeed, the addition of already small amount of tetralin leads to clearly improved printability of the ink as well as to printed blends with optimal drying behavior and homogeneous micro- and nanoscale morphology. However, compared with spin-coated blends, they show distinctive surface morphology. The successful optimization of ink composition and blend printing results in solar cells using inkjet-printed polymer blends with a maximum efficiency of 10.1% at an optimal layer thickness of 120 nm, whereas thick photoactive layers up to 400 nm still provide a performance of 8.4%. Systematical studies of structural, nanoscale, and electronic properties of the printed blends compared with spin-coated layers reveal that IJP leads to clear morphological changes in terms of donor material capping layer formation at the surface and improved phase separation and crystallinity for both donor and acceptors leading to low charge carrier recombination in thick blend layers.

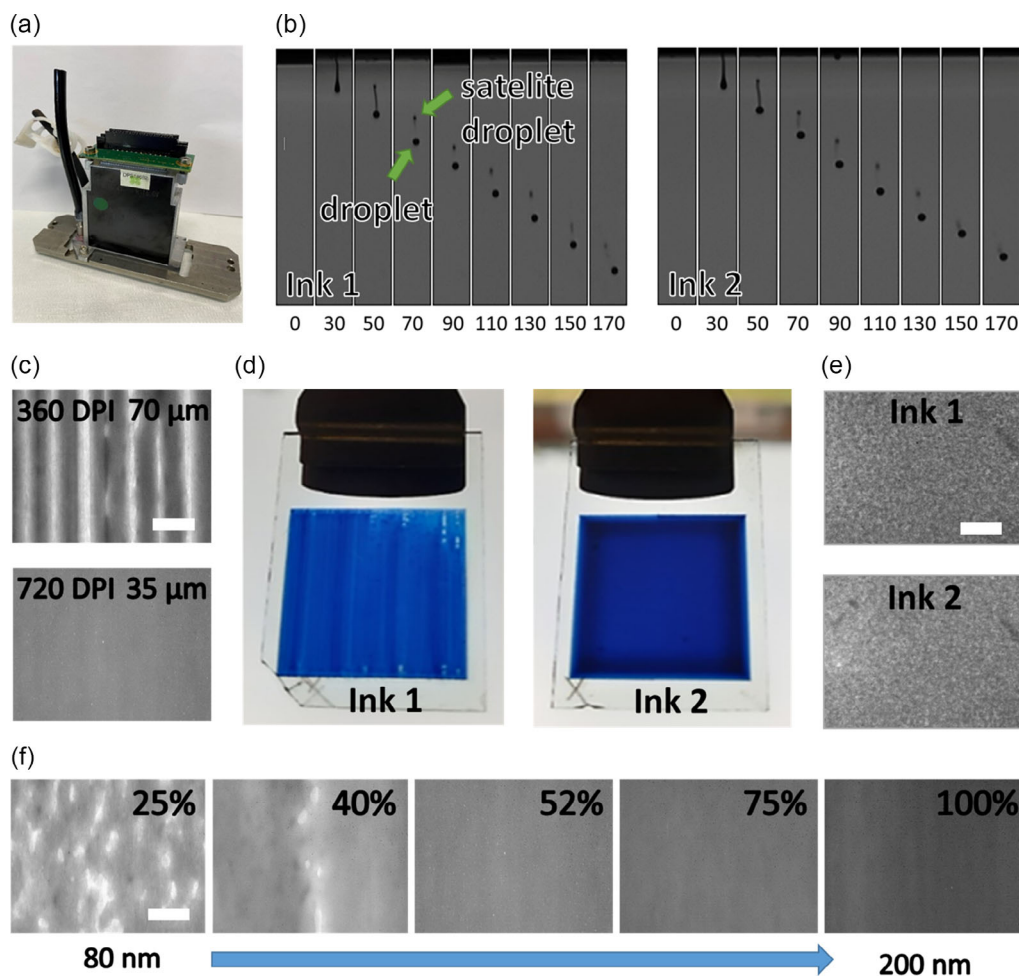
## 2. Printing of NFA Blends from Non-Chlorinated Solvents

A crucial part of the ink formulation process is the high solubility of the blend materials in the selected solvents to avoid the clogging of nozzles within the print head during processing through the formation of aggregates or a gel. We first tested the solubility of the blend based on PBDB-T, PM6, and ITIC as well as ITIC-4F in o-xylene, the chemical structures of which are shown in Figure 1b and Figure S1a, Supporting Information. The PM6, PBDB-T, ITIC-4F, and PM6:ITIC-4F blends dissolve in o-xylene already at room temperature at a concentration of  $10 \text{ mg mL}^{-1}$  without leaving any aggregates and form stable inks over days after initial stirring overnight. In contrast, the solubility of non-fluorinated ITIC was found much lower in o-xylene as dissolving ITIC in o-xylene leads to inks with the presence of large aggregates even after stirring over 12 h at  $80^\circ\text{C}$ . As shown in Figure S1 and Table S2, Supporting Information, spin-coated PBDB-T:ITIC layers show poor layer morphology with a high micro-sized surface roughness as seen already in optical microscopy analysis that leads to corresponding solar cells with strongly reduced performances compared with devices using layers processed with chlorobenzene. Thus, it is clear that the fluorination of ITIC-4F is essential to gain high solubility in o-xylene, allowing to obtain high-efficient polymer blends as shown before in the case of doctor-bladed layers.<sup>[32]</sup> We, thus, focused on the IJP of polymer blends using ITIC-4F as NFA in combination with PM6.

For the IJP of the photoactive layer, we selected two different ink formulations using ( $10:10 \text{ mg mL}^{-1}$ ) PM6:ITIC-4F solutions. The first one (ink 1) contains pure o-xylene as solvent, whereas the second (ink 2) is based on a mixture of o-xylene and tetralin as a high boiling temperature co-solvent. We selected tetralin as co-solvent at low concentration for several reasons. First, previous work on inkjet-printed P3HT:PC61BM blends has shown that a combination of low and high boiling point solvents such as

chlorobenzene using tetralin as co-solvent at 20% v/v ratio allows to avoid fast evaporation of the solvent during layer drying.<sup>[33]</sup> A mixture of o-xylene and tetralin was also applied to improve the printability of fullerene- and non-fullerene-based blends using o-xylene as main solvent.<sup>[12,22]</sup> To select the most suitable concentration, we processed solar cells using PM6:ITIC-4F inks with a tetralin concentration between 3.5% and 50% by SC. As shown in Table S3, Supporting Information, identical PCE was reached for all concentration studied, indicating a high compatibility and a low performance sensibility of the PM6:ITIC-4F blend on the concentration of tetralin as co-solvent. However, high boiling temperature solvents such as tetralin are difficult to be removed from the printed blend demanding the high temperature annealing processes that often decrease device performance. Considering that already small concentration of high boiling temperature solvent can improve the drying behavior during IJP,<sup>[34]</sup> we selected a low tetralin concentration of 3.5% (ink 2) to obtain suitable drying behavior by keeping the post-annealing temperature equal to  $70^\circ\text{C}$ . Interestingly, we also address here the question whether tetralin impacts directly on the NFA organization inside the blends as it would be expected in the case of a typical additive such as diiodooctane (DIO). To validate the printability of the inks based on NFA, we first determined viscosity, density, surface tension, and the dimensionless parameter Z developed by Fromm<sup>[25]</sup> and then investigated by Reis and Derby,<sup>[35]</sup> indicating the stability of the droplets generated from the ink during the jetting process. PM6:ITIC-4F-based ink 1 and ink 2 resulted in the Z values of 2.46 and 3.40, respectively (see Table S4, Supporting Information), indicating that both inks are suitable for IJP. The investigation of the drop jetting from the print head (Figure 2a) was done with a strike camera over a span of  $170 \mu\text{s}$ , as shown in Figure 2b. The presence of the satellite drop can be clearly seen at all time spans for ink 1, whereas in the case of ink 2, the satellite droplet vanished after  $170 \mu\text{s}$  generating a perfect droplet. The ONT for ink 1 is below 10 s, whereas for ink 2, droplets are sufficiently jetted over 30 s (see Figure S2, Supporting Information). This clearly shows that already a small amount of tetralin in the blend solvent mixture improves the overall jetting process and the robustness of the IJP, which can be attributed to the reduction of the vapor pressure of the ink upon the addition of tetralin.<sup>[34]</sup>

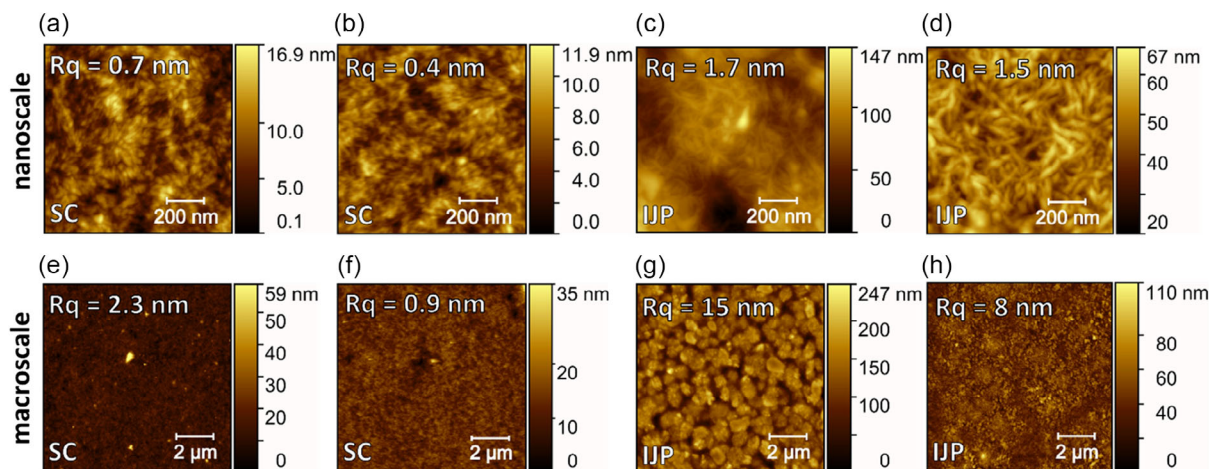
As a next step, we studied the layer quality of the printing of blend layers depending on two printing parameters. In contrast to lab scale printer, our semi-industrial printer uses the resolution of printing in dots per inch (DPI) to control the drop spacing (DS) and the amount of printed pixels (APP) to control layer thickness. More details are given in the Supporting Information. We investigated the impact of the ink formulation on the optical and morphological quality of the printed PM6:ITIC-4F layers using a DS of 35 and  $70 \mu\text{m}$ , respectively, while keeping the APP at 100%. As shown in Figure 2c, a DS of  $70 \mu\text{m}$  generates non-uniform layers as DS was too large to form closed layers during drying. In contrast, a DS of  $35 \mu\text{m}$  generates closely packed layers with a nominal thickness of  $\approx 200 \text{ nm}$  for both ink formulations. However, due to the short ONT and, as a result, fast nozzle clogging, non-uniform layers with defects were produced with ink 1. Only ink 2 leads to uniform blend layers of a large area of around  $3 \text{ cm}^2$ , as shown in Figure 2d. Nevertheless,



**Figure 2.** a) Photograph of the industrial print-head Konica Minolta KM512. b) Photographs of drop formation evolution for PM6:ITIC-4F ink 1 and ink 2 with the concentration of  $20 \text{ mg mL}^{-1}$ . Both ink droplets were jetted with an applied voltage of 19 V, 1 kHz frequency, and 14 mbar backpressure in the print head. Time in  $\mu\text{s}$  indicates the following of the droplet from 0 to 170  $\mu\text{s}$  after the voltage pulse. c) Optical microscope images of PM6:ITIC-4F inkjet-printed layers showing the impact of the DS of the IJP on the layer quality. d) Photographs of PM6:ITIC-4F inkjet-printed layers from ink 1 and 2; the printed area on the photograph corresponds to  $2 \text{ cm}^2$ . e) Optical microscope images of PM6:ITIC-4F inkjet-printed layers e) processed from ink 1 and ink 2, and f) showing the impact of the APP in the 720 DPI image on the layer quality and thickness of the layer for the blend casted from ink 2. Scale bars in panels (c,e,f) represent 1.5 mm.

at the millimeter scale, as shown in the optical images in Figure 2e, IJP of ink 1 demonstrated comparable layer quality to the layer processed from ink 2, allowing us still to process solar cells. We further varied the thicknesses from  $\approx 120$  to  $\approx 400$  nm of the layers processed from ink 2 by varying the APP and the number of printing steps. In all cases, high-quality layers were obtained, as shown in Figure 2f and Figure S3, Supporting Information. To study the influence of IJP on the layer morphology and micro- and nanoscale compared with films processed by SC, we first applied atomic force microscopy (AFM) analysis to visualize the surface morphology of spin-coated and inkjet-printed blends processed from the two ink formulations. All layers were deposited on ZnO + indium tin oxide (ITO)-coated glass substrates in identical conditions. Topography images together with root mean square ( $R_q$ ) roughness values of PM6:ITIC-4F layers deposited either by SC or IJP are shown in Figure 3. Inkjet-printed layers processed from both inks show a small increase in surface roughness up to 1.7 nm in

comparison with spin-coated layer (0.7 nm). Moreover, a fibril pattern is observed as surface morphology of printed PM6:ITIC-4F layers with the long chains of around 200 nm length (Figure 3c), whereas spin-coated layers show smaller “grain”-like patterns with a typical grain size of  $\approx 40$  nm (Figure 3a). While nanoscale morphology remains similar for the two inks, we observe a stark difference at a larger scale of  $10 \times 10 \mu\text{m}$ . Inkjet-printed layers processed from ink 1 are composed of large areas of  $\approx 1 \mu\text{m}$  size, which are divided by a 60 nm deep trench (Figure 3g and Figure S4d, Supporting Information), resulting in the  $R_q$  values of about 15 nm. In contrast, spin-coated layers show a homogeneous topography at this scale (Figure 3e). The morphology of the printed PM6:ITIC-4F layer processed from ink 2, which uses tetralin as co-solvent, is strongly improved compared with ink 1. Indeed, smooth layers without micro-sized domains are observed at microscale that are comparable to spin-coated ones (Figure 3d,h, respectively). Moreover, the printed layers processed with ink 2 demonstrate uniform and



**Figure 3.** a–d) AFM images of  $1 \times 1 \mu\text{m}$  showing topographies and root mean square roughness ( $R_q$ ) of PM6:ITIC-4F layers deposited by a) SC from ink 1, b) SC from ink 2, c) IJP from ink 1, and d) IJP from ink 2. e–g) The corresponding AFM images of  $10 \times 10 \mu\text{m}$ .

homogeneous surface morphology with an  $R_q$  of 8 nm independent of the layer thickness that is, however, increased in comparison with the spin-coated layers. In addition, we again observe fibril structures on the surface of the printed layers similar to ink 1 that are further enlarged when increasing layer thickness to 400 nm (see Figure S5, Supporting Information).

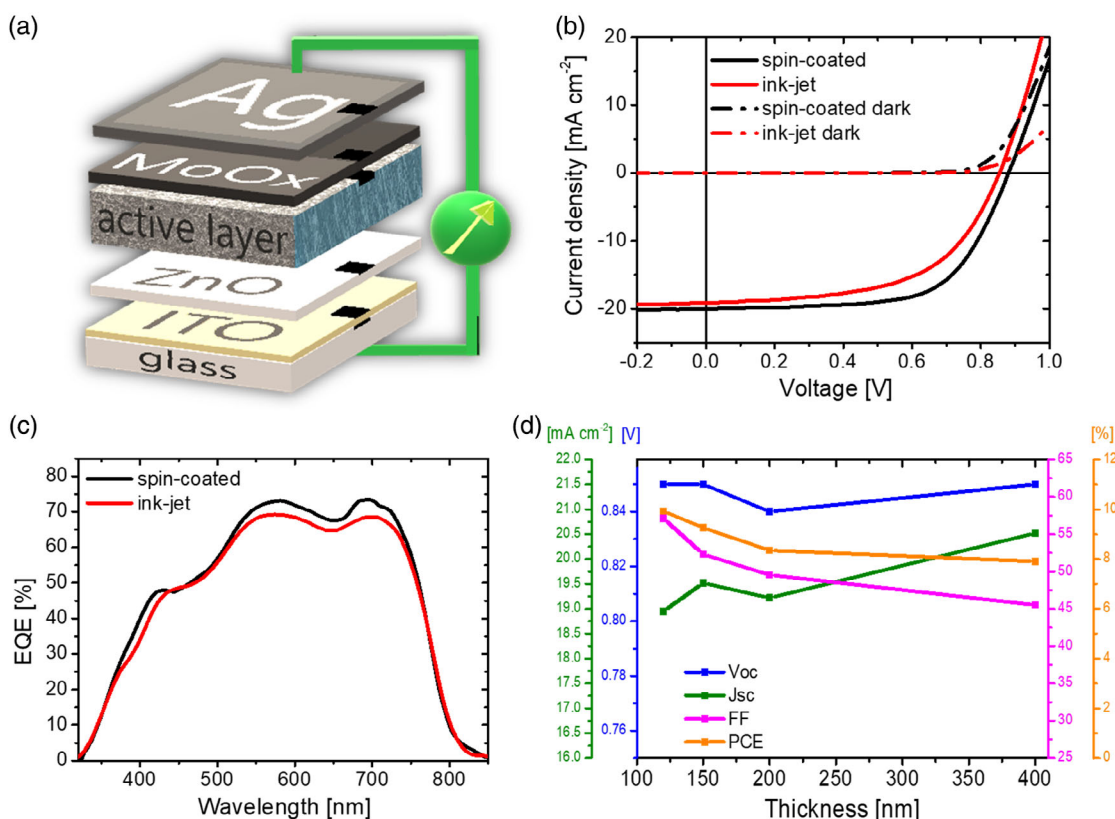
In conclusion, these results show that there is a complex interplay of the ink components and printing processes controlling the blend quality. Indeed, ITIC-4F and PM6 are highly soluble in *o*-xylene, which is essential for the stability of the ink as well as for the blend formation during drying, but not a sufficient condition for high-quality blend layers processed by IJP. The addition of the co-solvent tetralin is highly important for not only improving the IJP parameters such as ONT and droplet formation, but also improving the drying process of the inkjet-printed PM6:ITIC-4F layers. Because of the dual function of tetralin, homogeneous polymer blends up to 400 nm thicknesses were formed. In addition, we found that IJP changes the surface morphology at the nanoscale compared with spin-coated layers that needs further investigations to understand, in detail, the origin and composition of the fibril structures, which will be addressed in the following sections.

### 3. Performance of NFA-Based Solar Cells Inkjet Printed from Non-Chlorinated Solvents

The evaluation of the photovoltaic properties of the printed blend layers was performed by the manufacturing of solar cells with spin-coated and inkjet-printed active layers at different thicknesses in an inverted device structure, as shown in Figure 4a. Studying the size effects of the active area of the solar cells is also essential to evaluate the performance of device at large scale.<sup>[36]</sup> Here, we compare solar cells with an active area of sizes 0.27 and 0.08  $\text{cm}^2$  to estimate the impact of size variation on the device performance. The performance of the 0.27  $\text{cm}^2$  sized devices is discussed in the main text, whereas the photovoltaic parameters of the small-sized devices are given in the Supporting

Information. Spin-coated blends were processed and dried inside the glove box, and the corresponding solar cells were used as a reference. In contrast, inkjet-printed layers were processed and dried in air, with the use of an identical drying temperature of 70 °C, before transferring them to the argon-filled glove box. For comparison, we also performed SC of blends in air under identical conditions to the inkjet-printed layers.

Thus, we first studied the impact of ink formulation, i.e., the presence of tetralin as co-solvent, on the performance of devices using spin-coated blends. Table 1 and Table S5, Supporting Information, summarize the photovoltaic parameters as a function of ink formulation, layer thickness, and process conditions (under air or argon atmosphere). Solar cells processed from ink 1 with a nominal thickness of 100 nm and an active area of 0.27  $\text{cm}^2$  show the average PCEs of  $\approx 10.4\%$  (highest efficiency 10.8%). The use of ink 2 produces solar cells with the average PCEs of  $\approx 10.8\%$  (highest efficiency 11.27%), which are slightly improved compared with pure *o*-xylene due to a small increase in fill-factor (FF). Reducing the active area size to 0.08  $\text{cm}^2$ , which is close to typical area used in high-efficiency solar cells, leads mainly to an increase in FF for all devices, as shown in Table S6, Supporting Information, resulting in an average PCE of 11.21% (PCE<sub>max</sub> of 12.24%) for ink 1 and an average PCE of 11.07% (PCE<sub>max</sub> of 12.01%) for ink 2. We, furthermore, increased the concentration of tetralin gradually up to 50% v/v ratio. The photovoltaic parameters of the corresponding devices are shown in Table S3, Supporting Information, demonstrating that the presence of tetralin up to 50% in the ink formulation has no impact on the performance of the polymer blends. We only observed slightly higher average PCE value for concentration between 3.5% and 7%. To evaluate the impact of air processing on the performance, we fabricated solar cells using ink 2 by keeping air exposure of the spin-coated blend before and during the drying equally to IJP process. This change in blend processing leads only to a small reduction in  $J_{sc}$  and FF of around 2% compared with blend layers processed inside the glove box, as shown in Table S5, Supporting Information. We can, thus, conclude that the presence of tetralin as co-solvent within the ink



**Figure 4.** a) Schematic representation of solar cell architecture. b) JV curves and c) EQE spectra of best PM6:ITIC-4F-based devices comparing IJP and SC. d) Photovoltaic parameters of PM6:ITIC-4F inkjet-printed solar cells with different active layer thicknesses.

**Table 1.** Photovoltaic parameters of spin-coated devices based on PM6:ITIC-4F inks with different solvents and thicknesses. All the photovoltaic parameters are taken from at least ten devices with the active area of 0.27 cm<sup>2</sup>.

Ink formulation, thickness	$V_{oc}$ [V]	$J_{sc}$ [mA cm <sup>-2</sup> ]	FF	PCE [%]	$PCE_{max}$ [%]	$R_s$ [ $\Omega$ cm <sup>2</sup> ]	$R_{sh}$ [ $\Omega$ cm <sup>2</sup> ]
Ink 1, 100 nm	0.87 ± 0.004	20.01 ± 0.25	59.55 ± 0.48	10.40 ± 0.10	10.86	8.5	980.4
Ink 1, 200 nm	0.84 ± 0.005	18.56 ± 0.08	44.93 ± 0.39	6.96 ± 0.04	7.06	11.8	473.9
Ink 2, 100 nm	0.88 ± 0.003	19.94 ± 0.17	61.66 ± 0.57	10.76 ± 0.09	11.27	7.3	1158.7
Ink 2, 200 nm	0.85 ± 0.005	19.09 ± 0.29	48.65 ± 1.30	7.93 ± 0.34	9.19	9.7	401.6

formulation or air processing has negligible impact on the performance of solar cells using SC blends.

Hence, the impact of tetralin as co-solvent at 3.5% v/v concentration (ink 2) on the performance of solar cells using IJP photoactive blends was studied. The photovoltaic parameters are summarized in Table 2, whereas the corresponding  $J$ - $V$  curves are given in Figure S6, Supporting Information. Due to the morphological constrains of layers processed from ink 1, we first compare the device performance of the two inks at a thickness of 200 nm for which suitable layers could be processed with ink 1. Solar cells processed with blend using ink 1 show an average PCE of 3.94%, which is strongly reduced compared with SC devices with an average PCE of 6.96% (see Table 1). In contrast, devices printed from ink 2 using 200 nm thick photoactive layers show an average PCE of 8.00% ( $PCE_{max}$  of 8.35%) that is equal to spin-coated solar cells

with an average PCE of 7.93% ( $PCE_{max}$  of 9.19%, see Table 1). These results clearly show that in contrast to SC, tetralin as co-solvent strongly improves the photovoltaic parameters of the printed solar cells. We then further optimized the performance of the inkjet-printed solar cells using ink 2 by varying blend layer thicknesses. Table 2 and Figure 4d summarize the photovoltaic parameters of the corresponding printed solar cells. As expected, the highest performance is observed for devices using the thinnest blend layers. An average PCE of 9.1% ( $PCE_{max}$  of 9.93%) was obtained for the blend of 120 nm thickness (Figure 4b). Reduction of the active area size to 0.08 cm<sup>2</sup> further increased devices performance to an average PCE of 9.4% ( $PCE_{max}$  of 10.12%) due to an increase in the FF of  $\approx$ 59% (see Table S7, Supporting Information). These results clearly demonstrate the beneficial effect of dual function of tetralin in gaining high-quality-printed PM6:ITIC-4F layers,

**Table 2.** Photovoltaic parameters of PM6:ITIC-4F inkjet-printed solar cells processed from ink 1 and ink 2 with different active layer thicknesses. Averaged parameters are taken from at least ten devices with an active area of 0.27 cm<sup>2</sup>.

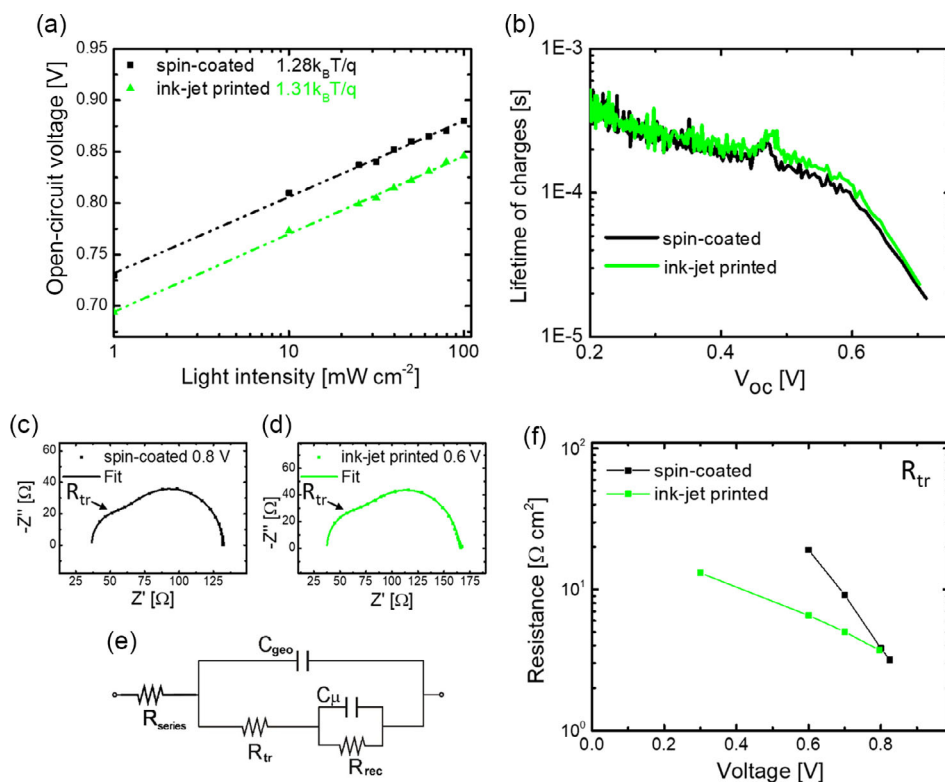
Ink formulation, thickness	$V_{oc}$ [V]	$J_{sc}$ [mA cm <sup>-2</sup> ]	FF	PCE [%]	PCE <sub>max</sub> [%]	$R_s$ [ $\Omega$ cm <sup>2</sup> ]	$R_{sh}$ [ $\Omega$ cm <sup>2</sup> ]
Ink 1, 200 nm	0.81 ± 0.005	10.35 ± 0.14	47.15 ± 1.07	3.94 ± 0.16	4.34	19.2	714.3
Ink 2, 200 nm	0.84 ± 0.007	19.22 ± 0.43	49.54 ± 2.28	8.00 ± 0.16	8.35	8.1	645.2
Ink 2, 120 nm	0.85 ± 0.004	18.95 ± 0.29	57.13 ± 1.58	9.1 ± 0.15	9.93	8.7	602.4
Ink 2, 150 nm	0.85 ± 0.003	19.52 ± 0.25	52.31 ± 0.81	8.72 ± 0.10	9.26	9.9	380.2
Ink 2, 400 nm	0.85 ± 0.003	20.52 ± 0.22	45.52 ± 1.58	7.91 ± 0.23	8.58	11.9	294.1

allowing to reach device performances over 10% for inkjet-printed solar cells using non-halogenated solvents that are close to the performance of spin-coated devices. Together with a very recent work of Corzo et al.<sup>[37]</sup> demonstrating inkjet-printed solar cells using PTB7-Th:IOICO-4F blends processed from non-halogenated solvent mixture with a PCE<sub>max</sub> of 9.8%, these results can be considered as an important step toward future commercialization of OSCs using industrial-relevant IJP processes (Figure 1a). Regarding the PCE trends as a function of blend thickness, we observe a different behavior to what was observed before for spin-coated devices,<sup>[31]</sup> i.e., a continuous decrease in  $V_{oc}$ , FF, and PCE, whereas  $J_{sc}$  increases first and then decreases. Indeed, the efficiency of inkjet-printed solar cells decreases when the layer thickness is increased from 120 to 200 nm, as expected. However, for 200 and 400 nm thick inkjet-printed layers, the performance is rather constant, leading to a PCE of 7.91% (PCE<sub>max</sub> of 8.58%, see Table 2) that can be addressed to a further increase in photocurrent for the 400 nm thick layer up to 20.54 mA cm<sup>-2</sup>. These results suggest that in contrast to SC, there are changes in the nanoscale morphology of inkjet-printed blends, leading to difference in charge carrier recombination as a function of thickness.

To better understand these changes, we compare the behavior of devices with photoactive layer processed by SC and IJP, respectively. By comparing photovoltaic parameters of solar cells using SC blends (Table 1) and inkjet-printed blends (Table 2), we see that the printed blend of 120 nm thickness leads to solar cells with clearly reduced FF compared with devices using spin-coated blends of comparable thickness of 100 nm. In addition, there is an increase in serial resistance of the spin-coated device of 7.3–8.1  $\Omega$  cm<sup>2</sup> for inkjet-printed blend layers, whereas the shunt resistance is decreased to 602  $\Omega$  cm<sup>2</sup> in comparison with 1158  $\Omega$  cm<sup>2</sup> of spin-coated cells. This may be the result of potential increase in charge carrier recombination and/or formation of leakage current in thin printed blends. In contrast, for 200 nm thick layers, we see that both serial and shunt resistances are almost equal for spin-coated and inkjet-printed blends, again suggesting that there may be improvement of the photovoltaic performance of printed blends with layer thickness. As the  $V_{oc}$  of solar cells depends fundamentally on the balance between charge carrier generation and recombination, the loss in  $V_{oc}$  also points toward increased charge carrier recombination. This can be caused by ITIC-4F aggregation during printing as recently shown for doctor-bladed PM6:ITIC-4F for which similar losses in  $V_{oc}$  were observed.<sup>[32]</sup> Indeed, the  $V_{oc}$  values are equal for both spin-coated and inkjet-printed blend layers at 200 nm

(see Table 1 and 2), supporting the fact that morphology of thicker printed layers was improved. The loss in  $J_{sc}$  is not only affected by charge carrier recombination losses, but it could be impacted by the variation of light absorption with the blend thickness. To study more in detail the photovoltaic properties of the two types of solar cells using PM6:ITIC-4F blend, we perform an external quantum efficiency (EQE) analysis. As shown in Figure 4c, the EQE spectra of inkjet-printed cells show a small drop over the whole absorption spectra of the blend compared with spin-coated devices, whereas the integration of the EQE with solar spectra supports the difference in a  $J_{sc}$  of 1 mA cm<sup>-2</sup>. We then addressed the difference in  $J_{sc}$  by simulating the amount of photons absorbed in the blend as a function of layer thickness. Indeed, there is a difference of 20 nm in layer thickness of optimized solar cells processed by SC (100 nm) and IJP (120 nm). As shown in Figure S7, Supporting Information, the theoretical optimum in blend thickness for the used device structure glass/ITO/ZnO/PM6:ITIC-4F/MoO<sub>3</sub>/Ag is around 90 nm. Beyond this value, the absorbed photon number inside the blend decreases constantly up to 155 nm. However, the difference in absorbed photons between 100 and 120 nm is relatively small that should vary  $J_{sc}$  only by 0.3%. We can, thus, address the loss in  $J_{sc}$  for optimized devices to increased charge recombination related to the nanoscale morphology.

The comparative investigation of  $V_{oc}$  values as a function of light intensity gives insight into the charge carrier recombination inside the polymer blends ( $n_{id}$ ).<sup>[38]</sup> Figure 5a plots the  $V_{oc}$  values as a function of light intensity and blend layer thickness. For optimized thin layer device, the ideality factor for inkjet-printed PM6:ITIC-4F layer is increased to 1.31 compared with 1.28 obtained for spin-coated layers (see Figure 5a), indicating that the recombination of charge carriers is slightly higher. Importantly, increasing layer thickness strongly improves the ideal factors of inkjet-printed blends. Indeed, the ideal factor at 200 nm reduces to 1.22 identically to that of solar cells using spin-coated blends, whereas further increase to 400 nm thickness results in solar cells with the very small values of 1.07 for IJP (see Figure S8, Supporting Information). To further study the difference in performance of solar cells using optimal layer thickness, we performed time-resolved  $V_{oc}$  decay measurements to extract charge carrier lifetimes. As shown in Figure 5b, solar cells with optimal thickness of photoactive layer processed by SC and IJP show similar lifetime profiles suggesting comparable charge carrier lifetimes in both devices. Furthermore, impedance spectroscopy (IS) under illumination was used to study charge transport in solar cells using both spin-coated and printed



**Figure 5.** a)  $V_{oc}$  dependence as a function of light intensity of spin-coated and inkjet-printed devices based on ink 2. b) The corresponding lifetimes of charge carriers determined from  $V_{oc}$  decay. c–f) Impedance response of PM6:ITIC-4F solar cells measured at 1 sun illumination close to  $V_{oc}$  conditions c) spin-coated device with 120 nm. d) Inkjet-printed active layer using ink 2 formulation with a thickness of 170 nm. e) Equivalent circuit to fit the spectra measured at different voltages: Series resistance ( $R_{series}$ ), geometrical capacitance ( $C_{geo}$ ), transport resistance ( $R_{tr}$ ), recombination resistance ( $R_{rec}$ ), and chemical capacitance ( $C_{\mu}$ ). f) Fitting results for transport resistance as a function of the applied voltage that highlights that morphology and transport are adequate for inkjet-printed devices.

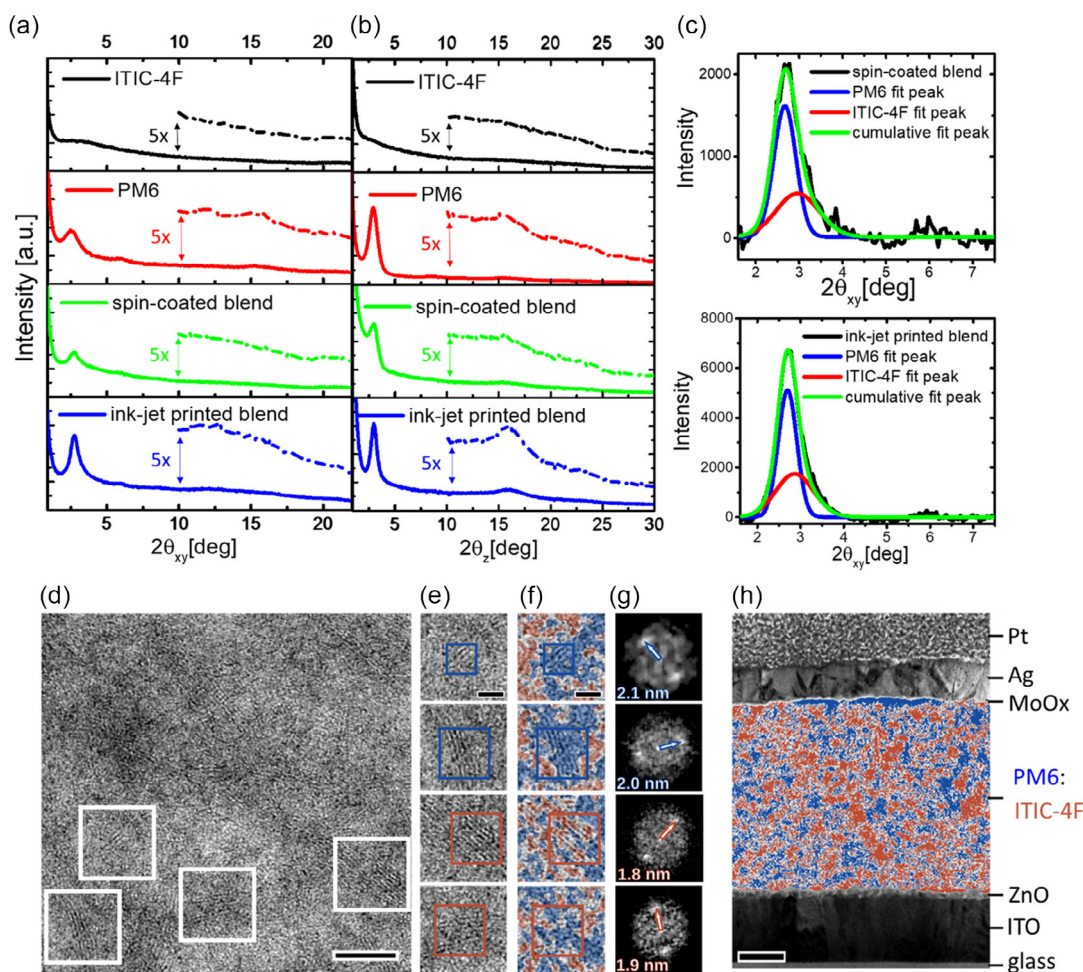
polymer blends. IS has been widely applied to organic photovoltaics based on fullerene<sup>[39–41]</sup> and NFA<sup>[42]</sup> small molecules. We compare optimized PM6:ITIC-4F devices using the two deposition methods, SC and IJP. At short circuit conditions,  $V = 0$ , both IS spectra demonstrate one arc previously correlated with the recombination resistance ( $R_{rec}$ ) and chemical capacitance ( $C_{\mu}$ ) of the device (see Figure S9, Supporting Information). Alternatively, at direct current bias approaching open circuit conditions (Figure 5c,d), a flat electrical field profile is expected between the contacts,<sup>[43]</sup> carriers are transported by diffusion, and a second arc set ( $R_{tr}$  and  $C_{geo}$ ) is observed in the IS spectra at high frequencies.<sup>[39]</sup> The presence of this second arc is a distinct feature of not fully optimized devices that points toward not optimized film morphology. The transport resistance arc can be fitted using a previously reported equivalent circuit (see Figure 5e). We observe that the  $R_{tr}$  values are low ( $\approx 10 \Omega$ ) and similar for spin-coated and printed devices at a given applied bias (Figure 5f) with small variations from batch to batch. Regarding the recombination resistance (Figure S9c, Supporting Information),<sup>[44]</sup> slightly higher recombination is observed for the inkjet-printed devices, which would account for the differences in  $V_{oc}$  for both devices. Hence, the difference in performance between solar cells manufactured by SC and IJP using optimal layer thickness may stem from difference in NFA organization

and the nanoscale morphology of the blends. However, as it was shown before, increasing layer thickness to 200 nm leads to equal performance between spin-coated and inkjet-printed devices, indicating that there are structural changes in IJP blends induced by the increase in layer thickness.

#### 4. Impact of IJP on Morphology and Crystallinity of the Polymer Blends

To understand deeper the performance difference of solar cells processed by either SC or IJP, we investigate nanoscale morphology, NFA ordering, and blend crystallinity of PM6:ITIC-4F with a set of advanced analysis techniques. To study NFA organization inside the blend, we first performed 2D grazing-incidence X-ray diffractometry (2D-GIXD) measurements on the neat layers of ITIC-4F and PM6 and blend layers made by SC and IJP from ink 2 using optimal layer thickness. In-plane (IP) and out-of-plane (OOP) profiles are shown in Figure 6a,b, whereas the corresponding patterns can be found in Figure S10, Supporting Information. Table S8 and S9, Supporting Information, provide the crystallization coherence length (CCL) of lamellar stacking obtained by fitting the (100) peak in IP and OOP (see Figure 6c and Figure S11, Supporting Information)





**Figure 6.** a) IP of line cut of 2D-GIXD with ITIC-4F, PM6 single compounds, and PM6:ITIC-4F blend casted by SC and IJP. b) OOP line cut of 2D-GIXD with the corresponding materials and blend. c) Gaussian fitting of the IP (100) peak of the spin-coated and inkjet-printed layers. d–g) Correlative TEM/ATEM analysis of crystalline areas within a PM6:ITIC-4F layer processed with ink 2. d) Bright-field TEM image of a PM6:ITIC-4F layer showing a semi-crystalline structure. The squares mark crystalline regions, which are exemplary taken for the analysis in (e). Scale bar represents 30 nm. e) Example regions selected from the image in (d) showing semi-crystalline areas. Scale bar represents 10 nm valid for all images in column. The squares mark crystalline areas, which are analyzed in (f,g). f) Overlay of the images in (e) and the corresponding material distribution map obtained by ATEM. The crystals inside the squares are assigned to specific material phases by ATEM. g) Power spectra of the marked regions in (e,f) showing small but significant variations in lamellar spacing for crystals in the donor and acceptor phases. h) Cross-sectional view of a 35 nm lamella showing an overlay of a bright-field TEM image showing the inorganic device layers above and below the active layer and a material distribution map obtained by ATEM of an inkjet-printed 400 nm active layer in between. Scale bars in panels (d,h) represent 100 nm.

according to the Scherrer equation,<sup>[45]</sup> which indicates the mean size of ordered (crystalline) domains.<sup>[46]</sup> For the pure layer of ITIC-4F, a weak and broad (100) lamellar peak is observed in the IP direction, indicating that the acceptor molecules are primarily organized in an amorphous phase. In case of neat PM6 layers, the IP profile shows a strong (100) peak around  $0.27 \text{ \AA}^{-1}$  ( $2.67^\circ$ ) corresponding to a  $d$ -spacing of  $\approx 22 \text{ \AA}$ . Moreover, the OOP profile shows a sharp and even more intensive (100) peak at  $0.31 \text{ \AA}^{-1}$  ( $2.58^\circ$ ) corresponding to a  $d$ -spacing of  $\approx 22 \text{ \AA}$  and weak (010) peak at  $\approx 1.7 \text{ \AA}^{-1}$  ( $15.3^\circ$ ) corresponding to a  $\pi$ - $\pi$  stacking of  $\approx 3.8 \text{ \AA}$ , implying a face-on dominated molecular orientation with respect to the substrate.<sup>[30]</sup> The calculated CCL of pure PM6 is 5.8 nm in the IP profile. When PM6 is blended with ITIC-4F, the lamellar (100) peak in the IP spectrum of

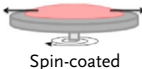
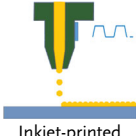
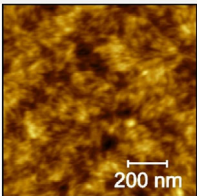
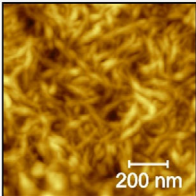

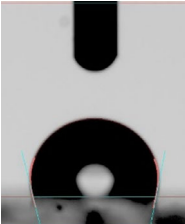
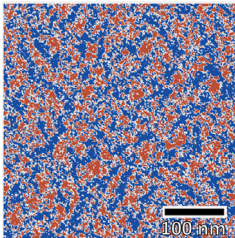
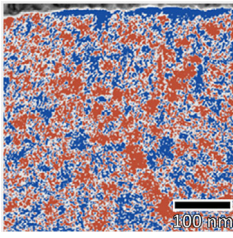
spin-coated and inkjet-printed layers is enlarged and accompanied by the appearances of new peaks mainly visible in the IP spectra of blend layers, as shown in Figure 6a,b. The Gaussian fitting of the (100) peaks of spin-coated and inkjet-printed layers reveals that there are two populations of crystalline organization in the blend with a  $d$ -spacing of 19.4 and 20  $\text{ \AA}$ . This clearly differs from the  $d$ -spacing of 22  $\text{ \AA}$  found in pure PM6 layers. The CCLs calculated from IP spectra of spin-coated and inkjet-printed blends are 8.6 and 10.2 nm for PM6 as well as 4.5 and 5.0 nm for ITIC-4F, proving a stark increase in crystallinity and crystalline domain size of both donor and acceptor in the polymer blends, whereas IJP slightly further increases the size of both domains. To gain more information about the changes in crystalline organization of both donor and acceptor

in the blend, we analyzed the PM6:ITIC-4F blends with analytic transmission electron microscopy (ATEM). We have recently shown that ATEM allows to obtain the unique insights into blend morphology based on ITIC such as material distribution of a polymer:NFA bulk heterojunction and, more importantly, NFA polymorphism inside the blend.<sup>[47]</sup> More details on processing and analyzing data by ATEM as well as the electron energy spectra of pure PM6 and ITIC-4F and the maps of segmented material phases are provided in Figure S12 and S13, Supporting Information. We first perform the bright-field TEM analysis of a spin-coated PM6:ITIC-4F layer, as shown in Figure 6d–g. Interestingly, we observe that the blend contains ITIC-4F crystals in contrast to pure spin-coated ITIC-4F layers. Thus, the differences between the IP spectra from XRD of neat and blend layers can be clearly addressed to a tendency of ITIC-4F to form more crystalline organization inside the blend. As the crystal size and spacing obtained from the (100) peak in the IP spectra (see Table S8, Supporting Information) are comparable for spin-coated and inkjet-printed layers, we can assume the similar molecular arrangement of ITIC-4F in both layers. Moreover, the long range molecular organization of ITIC-4F inside both blends is similar to the one observed in doctor-bladed layers of ITIC-4F-based blends.<sup>[48]</sup> While neat ITIC-4F layers show an amorphous structure, both 2D-GIXD and electron diffraction measurements from ATEM analyses of the polymer blends show a broad signal in the range from 18 to 21 Å corresponding to different ITIC-4F ordering (Table S8 and S10, Supporting Information) and, thus, proving near-order molecular arrangement between ITIC-4F molecules (see Figure 6a,b and Figure S14, Supporting Information). A statistical overview of the amount of PM6 and ITIC-4F crystals in the blend is summarized in Table S10, Supporting Information, revealing a sharp increase in crystallinity of ITIC-4F inside the blend. The dominant lamellar spacing corresponds to the 2.1 and 1.95 nm signals as obtained from the 2D-GIXD measurements and can be, thus, clearly addressed to the two organization populations, one corresponding to PM6 lamellar structures, whereas the second arises from ITIC-4F crystals. Based on these results, we conclude that acceptor crystallization induced by the polymer occurs for PM6:ITIC-4F blends that appears to be typical for PBDB-T:ITIC blend systems and their derivatives.<sup>[47]</sup> The identified *d*-spacing for PM6 and ITIC-4F is very close to those recently measured in a PM6:ITIC-4F blend.<sup>[49]</sup> We then used ATEM to visualize the material distribution maps of inkjet-printed and spin-coated blend layers. For top view, imaging of polymer blend is necessary to process thin blend layers of typically 40 nm thickness. This was only possible using SC, whereas IJP only results in suitable layers with a thickness higher than 100 nm. Therefore, we could visualize the morphology of spin-coated layers in a top-view configuration only. Nevertheless, the top-view analysis was used to clarify the role of tetralin in the layer formation in the case of spin-coated blends. By the fact that we only use 3.5% of tetralin in ink 2, tetralin might also be treated as solvent additive normally used to improve solubility of the acceptor in polymer blends.<sup>[50]</sup> Figure S12 and S13, Supporting Information, show the material distribution maps obtained by ATEM of spin-coated PM6:ITIC-4F blend processed from ink 1 and ink 2. It can be seen that both layers show identical morphology composed of homogeneously distributed ITIC-4F domains

between 5 and 10 nm embedded in the PM6-enriched phase separated by a thin mixed phase. This proves that tetralin can be purely considered as co-solvent controlling only printability and drying behavior of the films and not the resulting nanoscale morphology. To get insight into the nanoscale morphology of inkjet-printed blend, ATEM cross section of a complete solar cell was performed. Figure 6h shows the ATEM cross section of the complete solar cells using a 400 nm thick inkjet-printed blend. It can be seen that PM6 and ITIC-4F are still homogeneously distributed throughout the whole photoactive layer, but the NFA domain sizes are clearly enlarged to sizes from 10 to 20 nm comparable to the ones observed in spin-coated layers (see Figure S12 and S13, Supporting Information). In addition, a 10–15 nm thick pure PM6 phase is observed at the surface of the polymer blend at the interface with the MoO<sub>3</sub> interfacial layer. This observation may be related to the appearance of fibril structures on the surface of inkjet-printed blends as observed in AFM surface analysis (see Figure 3d), suggesting that IJP layers form polymer-enriched surface layers. To validate this interpretation, using Cassie's equation,<sup>[51]</sup> it is possible to approximate the amount of donor and acceptors at the surface of the blend by contact angle measurements of water droplets on spin-coated and inkjet-printed polymer blends.<sup>[37]</sup> Following from the contact angles obtained for pure PM6, ITIC-4F, and the corresponding spin-coated and inkjet-printed blends, respectively (see Figure S15, Supporting Information), we calculated the approximate fraction of the materials on the surface of each blend. Thus, the surface composition of SC blend is 66.58% of ITIC-4F and 33.42% of PM6, respectively (see Table S11, Supporting Information). In contrast, the fraction of ITIC-4F on the surface of printed blend is 22.02%, whereas 77.98% of the surface is covered by PM6. These results point toward a strong impact of the layer processing technique on the blend surface and support our interpretation of a polymer capping layer in the case of inkjet-printed blends. Considering that the size of the fibril structure on the blend layers observed by AFM is increased when the layer thickness increases, we deduce that morphological changes in terms of NFA domain size and thickness of the capping layer within the inkjet-printed blends are enhanced. Compared with SC that leads to fast drying of the blend layer independently of the layer thickness, there is increased amount of solvent with increasing layer thickness in the case of IJP, which results in slower drying kinetics and, thus, in more pronounced phase separation.

From the detailed morphological analyses, we show that there are distinctive differences in surface and bulk morphology between inkjet-printed and spin-coated layers that are summarized in Table 3. We observe the formation of a PM6 capping layer for IJP that is potentially highly favorable for efficient hole extraction in solar cells using inverted device architecture. Furthermore, there is an increase in phase separation inside the blend. Both changes indicate a stronger demixing of donor and acceptor during the IJP process. Furthermore, we show that the crystalline ordering of ITIC-4F is enhanced inside the blend for both deposition techniques compared with neat layers; however, this ordering is further increased during IJP together with a higher ordering of PM6 and accompanied by a change in *d*-spacing in ITIC-4F domains. Thus, there is a formation of a more favorable blend morphology in the case of IJP compared with SC. It has to be stated that this morphology depends on

**Table 3.** Morphological overview of PM-6:ITIC-4F spin-coated and inkjet-printed solar cells processed from ink 2 based on AFM, contact angle, ATEM, and 2D-GIXD analysis.

Parameter	 Spin-coated	 Inkjet-printed
Roughness [nm]	0.7	1.7
Surface structures	 "grains" 200 nm	 "fibrils" 200 nm
Size of surface structures [nm]	30	200
Fraction of the PM6 on the surface [%]	33.4	77.9
ITIC domain sizes [nm]	 5-10	 10-20
PM6 capping layer thickness [nm]	 100 nm	 100 nm
PM6 <i>d</i> -spacing IP [nm]	–	15-30
ITIC-4F <i>d</i> -spacing IP [nm]	2.15	2.14
ITIC-4F <i>d</i> -spacing IP [nm]	1.94	2.00
PM6 CCL IP [nm]	8.6	10.2
ITIC-4F CCL IP [nm]	4.5	5.0
<i>d</i> -spacing OOP [nm]	2.15	2.14
CCL OOP [nm]	5.3	8.1

the individual solubility properties of the selected donor and acceptors, and, in our case, it is directly correlated with the high solubility and the suitable balance in drying and crystallization kinetics of PM6 and ITIC-4F. All the common observed features show that the slower drying of inkjet-printed layers can lead to a significant improvement in the nanoscale morphology of the blend. In particular, the formation of a PM6-enriched surface together with strongly reduced charge carrier recombination in thick blend makes inkjet-printed photoactive layers very promising for industrial applications.

## 5. Conclusion

IJP is considered as a promising technique for processing of shape-controlled digital-printed OSCs. Due to the generally higher complexity of this technique compared with deposition technique such as SC or doctor blading, the efficiencies of such printed solar cells are usually significantly lower, especially when considering the use of non-halogenated solvents for the printing of the blend. In this work, inks based on highly efficient donor polymers and NFAs in non-halogenated solvents were developed

to process highly efficient solar cells by IJP. A special focus was put on investigating morphological differences between spin-coated and printed blend layers and correlating these differences with the solar cell efficiencies. For this purpose, typical ink jetting tests together with a set of advanced characterization techniques including 2D-GIXD, ATEM, and IS were used. Our work revealed that there is a complex balance between donor and acceptor solubility, ink formulation, and printing processes to obtain suitable blend morphology by IJP. Indeed, the high solubility of both PM6 and ITIC-4F in *o*-xylene was found to be essential but not sufficient to process layers with suitable nanoscale morphology. We show the importance of tetralin as a multifunctional co-solvent to reach highly efficient polymer blends. Indeed, tetralin not only improves jetability and ONT during the inkjet process, but also optimizes the layer drying process resulting in nano- and microscopically smooth layers. Using optimal printing conditions leads to polymer solar cells with the maximum efficiencies up to 10.1%. The comparison of the morphology of spin-coated and inkjet-printed blend layers reveals that IJP introduces distinctive changes on the blend surface as well as in the phase separation and crystallinity of both donor and acceptor in the volume. Especially, the formation of a thin PM6 capping layer on the blend surface together with strongly reduced charge carrier recombination in thick blends points to a high potential of IJP for industrial applications. Further work will address a deeper understanding of the blend formation under slow drying to further increase the efficiency of inkjet-printed polymer solar cells. This should go in line with the design of suitable donor and acceptor pairs with well-balanced blend miscibility and crystallization kinetics.

## 6. Experimental Section

**Materials:** Patterned ITO substrates with the dimensions of 20 mm × 30 mm and 15 Ω cm<sup>-2</sup> were purchased from Lumtech, Taiwan. ZnO ink (2.5% weight percentage in 2-propanol) was purchased from Avantama. Chlorobenzene, *o*-xylene, 1,2,3,4-tetrahydronaphthalene (tetralin), and molybdenum (VI) oxide (MoO<sub>3</sub> purity 99.97%) were purchased from Sigma-Aldrich. PM6, PBDB-T, ITIC, and ITIC-4F were purchased from 1-material (the values of the molecular weight of the polymers were not provided by the company).

**Device Fabrication:** The solar cells were manufactured with an inverted architecture: glass/ITO/ZnO/active layer/MoO<sub>3</sub>/Ag. First, the ITO substrates were thoroughly cleaned by sonication in acetone and ethanol followed by rinsing with water and sonication in isopropanol for 10 min in each solvent and applying UV ozone for 15 min at 80 °C. A thin layer of ZnO was spin-coated on the cleaned ITO pre-coated glass substrate in the ambient conditions at a speed of 5000 rpm for 60 s followed by heating on a hot plate at 120 °C for 10 min. Two different blend solutions of PBDB-T/ITIC or PM6:ITIC-4F for the photoactive layer were used: 1) (10:10 mg mL<sup>-1</sup>) in *o*-xylene and 2) (10:10 mg mL<sup>-1</sup>) in (96.5% volume) *o*-xylene and (3.5% volume) tetralin. All the inks were stirred at room temperature overnight. The PM6:ITIC-4F layers were inkjet printed in ambient conditions on top of the ZnO using a printer Ardeje OriginD100 (CINaM) and Ardeje OriginD200 (Dracula Technologies) with Konica Minolta print head (512 nozzles) and dried at 70 °C for 2 min in ambient conditions. For the sake of comparison, the printing parameters were set identically: the applied voltage of 19 V, 1 kHz ejection frequency, and 14 mbar meniscus pressure in the print head. For the comparison, the PBDB-T/ITIC and PM6/ITIC-4F layers were spin-coated inside of argon-filled glove box and in the ambient conditions at 2200 rpm for 60 s with the subsequent annealing at 70 °C for 2 min, resulting in layers with the nominal thickness

of 100 nm. To complete devices, 2 nm of MoO<sub>3</sub> and 100 nm of Ag were thermally evaporated at 1 × 10<sup>-7</sup> mbar through a shadow mask to obtain a device area of 0.27 cm<sup>2</sup>.

**Characterization:** The current density–voltage (*J*–*V*) characteristics of the devices were measured using a Keithley 238 Source Measure Unit inside the glove box. Solar cell performance was measured using a Newport class AAA 1.5 Global solar simulator (Oriol Sol3ATMmodel no. 94043A) with an irradiation intensity of 100 mW cm<sup>-2</sup>. The light intensity was determined with a Si reference cell (Newport Company, Oriol no. 94043A) calibrated by the National Renewable Energy Laboratory (NREL). The EQE of the solar cells was measured using a 150 W Xenon arc lamp along with Oriol Cornerstone 260 monochromator. The setup was calibrated with Si diode from Newport Company. The open-circuit voltage decay (OCVD) measurement was performed by illuminating the device at open circuit and then observing the voltage decay as carriers recombine when the illumination is turned off. The devices were illuminated by driving the white light emitting diode (LED) with square wave pulses. The LED input and solar cell output were synchronized and recorded by the oscilloscope (Agilent). The absorbance of the active layer films was measured by UV–Vis–near infra-red Spectrophotometer Cary 5000. The surface morphology of the blend layers was investigated by AFM (NTEGRA from NT-MDT) in tapping mode using the silicon tips (MikroMash) with a theoretical resonant frequency of 300 kHz and a spring constant of 16 N m<sup>-1</sup> at room temperature. The quality of the printed layers was analyzed by optical microscope DMK Nikon. Film thicknesses were measured by a stylus profilometer (Bruker DEKTAK XT) with a 1 mg force on the probing tip. Viscosity of the inks was measured by Brookfield cone/plate rheometer (DVNXLV) at 22 °C. Surface tension of the inks and contact angle measurements of the films were measured by an optical contact angle system OCA 20 (DataPhysics Instruments) using a pendant drop method within the SCA software at 20 °C. The drop jetting of the printer was done with a stroboscopic flash system and a conventional digital camera operating in a standard video mode. Polymer blends were further analyzed by 2D-GIXD with high-brightness synchrotron radiation at BL19B2 in SPring-8. The 2D-GIXD measurements were performed using a high-sensitive 2D X-ray detector (PILATUS 300 K). The incident angle and wavelength of X-rays were 0.13° and 0.100 nm, respectively. IS measurements were performed using an Autolab PGSTAT-30 equipped with a frequency analyzer module. Measurements were carried out at 1 sun light illumination conditions without using the masks to avoid creation of different areas that can contribute to the impedance of the sample. A small AC voltage perturbation of 20 mV (root mean square) was applied to keep the linearity of the response.

To determine the optimal thicknesses of the photoactive blends for the maximum photocurrent generation, ellipsometry was used to extract the optical indices of neat PM6 and ITIC-4F and PM6:ITIC-4F-blended thin films. The measurements were performed for wavelengths ranging between 380 and 1000 nm using a Semilab rotating compensator ellipsometer equipped with a microspot, which focuses the beam on a very small area of the sample (a circle with a diameter of 100 μm). The layers were coated on glass substrates. SEA software (Semilab company) was used to fit the spectroscopic ellipsometry measurements of tan(Ψ) and cos(Δ) and extract the optical indices *n*(λ) and *k*(λ) of the materials. The dielectric functions  $\epsilon = \epsilon_1 + i \times \epsilon_2$  of blend systems were fitted with the Gaussian model that is adequate for the parameterization of the optical functions of amorphous thin films in the interband region.<sup>[52]</sup>

**Preparation and Characterization of Samples for ATEM:** The pure material layers (PM6 and ITIC-4F) and the spin-coated photoactive layers of the blend system PM6:ITIC-4F were floated upon demineralized water by dissolving the poly(3,4-ethylenedioxythiophene) polystyrene sulfonate layer and collected with holey carbon grids (QUANTIFOIL).

From a solar cell device with printed active layer, two lamellae with six windows were prepared using a ZEISS Crossbeam 540 (Carl Zeiss Microscopy GmbH, Germany). On three of six lamella windows, the TEM analysis was performed as described in the next paragraph. The lamella preparation was performed in four steps. First, platinum was deposited on a specified area to protect the device layers against high energy gallium ions during the subsequent milling steps. Second, a lamella with a thickness of 2 μm was cut out at the region with the platinum

deposition on top using gallium ions at emission currents in the range of 15 nA and 300 pA at an acceleration voltage of 30 kV. In the third step, the lamella was lifted out with a micromanipulator (Kleindiek Nanotechnik GmbH, Germany) and welded on a copper lift-out grid (OmniProbe). The lamella was thinned down for subsequent TEM analysis to a thickness of 35 nm with gallium ions at an emission current of 5 pA and an acceleration voltage of 5 kV for TEM analysis. Before transferring the lift-out grid to the TEM, the lamella surface was showered with gallium ions at an emission current of 10 pA and an acceleration voltage of 2 kV.

TEM, electron energy loss spectroscopy (EELS), and electron spectroscopic imaging (ESI) measurements were performed with a Cs aberration-corrected Libra 200 MC (Carl Zeiss Microscopy GmbH, Germany) at 60 kV. The microscope is equipped with an in-column energy filter and monochromator. EEL spectra were recorded from pure layers PM6 and ITIC-4F with a thickness of around 35 nm and an energy resolution of 75 meV. The EEL spectra were deconvoluted by Fourier-log deconvolution<sup>[53]</sup> and normalized by the integral from 1 to 40 eV using HyperSpy.<sup>[54]</sup> For first EELS acquisition, a total electron dose of 3000 electrons per nm<sup>2</sup> was applied. After a total dose of 6000 electrons per nm<sup>2</sup>, the bandgap signal below 5 eV vanished by irradiation damage. For the same reason, the signal at 6.5 eV of ITIC-4F changed after a total dose of 45 000 electrons per nm<sup>2</sup>. However, the plasmon signals of both materials above 10 eV showed a much higher dose tolerance with negligible changes even after  $5 \times 10^9$  electrons per nm<sup>2</sup>, which was used to generate material contrast in the ESI images. The corresponding spectra is found in Figure S10, Supporting Information.

ESI images were acquired from spin-coated PM6:ITIC-4F blend layers and from three of six lamella windows for cross-sectional view of an IJP solar cell device using the same material system as a photoactive layer. ESI image series were recorded from 5 to 45 eV in the steps of 1 eV, whereas the slit aperture for inelastic images was set to a width of 1 eV. Using the same slit aperture of 1 eV, an additional energy-filtered TEM image at 0 eV was recorded before each (energy-filtered) inelastic image to improve phase contrast. The first TEM image was taken from spin-coated layers before initial damage is induced to the sample position. The TEM image of the undamaged sample position was later used for correlative TEM/ATEM overlay with the resulting material distribution map as described in the next paragraph. The other TEM images were used for image alignment of the corresponding ESI image stack. The total dose for each series was approximately  $6 \times 10^6$  electrons per nm<sup>2</sup>.

The inelastic images from the ESI series were aligned by affine image registration and normalized by the sum of all inelastic images in the series to remove the thickness and density contrast in the images revealing material contrasts. Principal component analysis was applied on the normalized ESI image stacks for noise reduction using Hyperspy.<sup>[54]</sup> Image classification and segmentation were done by statistical analysis and supervised machine learning using the open source software ilastik<sup>[55]</sup> to classify the ESI spectra into distinct classes. By applying locally linear embedding (LLE), the dimensionality of the data was reduced. Afterward, a random forest classifier was trained on label subsets and subsequently used to classify the remaining spectra (all pixels/spectra of the image stack) yielding material distribution maps of PM6 and ITIC-4F in blend layers showing material domains and interface phases. We note that the LLE is implemented in several free-of-charge software, e.g., in Matlab (MathWorks, USA) or in Python with the scikit-learn package. Detailed information on this method can be found elsewhere.<sup>[56]</sup> The Fourier-log-ratio method was used to measure the layer thickness in the TEM.<sup>[53]</sup>

## Supporting Information

Supporting Information is available from the Wiley Online Library or from the author.

## Acknowledgements

P.P., J.-J.S., and J.A. received funding from the European Union's Horizon 2020 research and innovation program under the Marie Skłodowska-Curie Grant Agreement No. 713750. W.K., M.P., and R.R.S. acknowledge funding by the Ministry of Science, Research and the Arts Baden-Württemberg, through the HEiKA materials research center FunTECH-3D (MWK, 33-753-30-20/3/3). P.P. and J.A. further acknowledge support of the Regional Council of Provence-Alpes-Côte d'Azur, A\*MIDEX (No. ANR-11-IDEX-0001-02), and the Investissements d'Avenir project funded by the French Government, managed by the French National Research Agency (ANR). This work has also been carried out within the framework of a CIFRE PhD grant 2017/0529 from the Association Nationale de la Recherche et de la Technologie (ANRT) and the Ministère de l'Enseignement Supérieur, de la Recherche et de l'Innovation, awarded through the company Dracula Technologies (Valence, France). The synchrotron radiation experiments were performed at BL19B2 in SPring-8 with the approval of Japan Synchrotron Radiation Research Institute (JASRI) (Proposal Nos. 2018B1791 and 2019B1851). R.R.S. also acknowledges funding by the Deutsche Forschungsgemeinschaft (DFG, German Research Foundation) under Germany's Excellence Strategy via the Excellence Cluster 3D Matter Made to Order (EXC-2082/1 – 390761711). W.K., R.R.S., and M.P. acknowledge the data storage service SDS@hd supported by the Ministry of Science, Research and the Arts Baden-Württemberg and the German Research Foundation (DFG) through grant INST 35/1314-1 FUGG. A.G. and H.B. thank University Jaume for the financial support (UJI-B2020-49).

## Conflict of Interest

The authors declare no conflict of interest.

## Data Availability Statement

Research data are not shared.

## Keywords

inkjet printing, non-fullerene acceptors, non-halogenated solvents, organic solar cells

Received: December 2, 2020

Revised: January 24, 2021

Published online: March 8, 2021

- [1] Y. Cui, H. Yao, J. Zhang, K. Xian, T. Zhang, L. Hong, Y. Wang, Y. Xu, K. Ma, C. An, C. He, Z. Wei, F. Gao, J. Hou, *Adv. Mater.* **2020**, *32*, 1908205.
- [2] S. Li, L. Zhan, Y. Jin, G. Zhou, T. Lau, R. Qin, M. Shi, C. Li, H. Zhu, X. Lu, F. Zhang, H. Chen, *Adv. Mater.* **2020**, *32*, 2001160.
- [3] I. Mathews, S. N. Kantareddy, T. Buonassisi, I. M. Peters, *Joule* **2019**, *3*, 1415.
- [4] Y. Cui, H. Yao, J. Zhang, T. Zhang, Y. Wang, L. Hong, K. Xian, B. Xu, S. Zhang, J. Peng, Z. Wei, F. Gao, J. Hou, *Nat. Commun.* **2019**, *10*, 2515.
- [5] H. Sun, T. Liu, J. Yu, T.-K. Lau, G. Zhang, Y. Zhang, M. Su, Y. Tang, R. Ma, B. Liu, J. Liang, K. Feng, X. Lu, X. Guo, F. Gao, H. Yan, *Energy Environ. Sci.* **2019**, *12*, 3328.
- [6] F. C. Krebs, *Sol. Energy Mater. Sol. Cells* **2009**, *93*, 465.

- [7] B. Zimmermann, H.-F. Schliep, M. Niggemann, U. Würfel, *Sol. Energy Mater. Sol. Cells* **2011**, 95, 1587.
- [8] M. Helgesen, J. E. Carlé, F. C. Krebs, *Adv. Energy Mater.* **2013**, 3, 1664.
- [9] S. Jung, A. Sou, K. Banger, D.-H. Ko, P. C. Y. Chow, C. R. McNeill, H. Siringhaus, *Adv. Energy Mater.* **2014**, 4, 1400432.
- [10] T. M. Eggenhuisen, Y. Galagan, A. F. K. V. Biezemans, T. M. W. L. Slaats, W. P. Voorthuizen, S. Kommeren, S. Shanmugam, J. P. Teunissen, A. Hadipour, W. J. H. Verhees, S. C. Veenstra, M. J. J. Coenen, J. Gilot, R. Andriessen, W. A. Groen, *J. Mater. Chem. A* **2015**, 3, 7255.
- [11] F. Hermerschmidt, P. Papagiorgis, A. Savva, C. Christodoulou, G. Itskos, S. A. Choulis, *Sol. Energy Mater. Sol. Cells* **2014**, 130, 474.
- [12] T. M. Eggenhuisen, Y. Galagan, E. W. C. Coenen, W. P. Voorthuizen, M. W. L. Slaats, S. A. Kommeren, S. Shanmugam, M. J. J. Coenen, R. Andriessen, W. A. Groen, *Sol. Energy Mater. Sol. Cells* **2015**, 134, 364.
- [13] E. Tekin, B.-J. de Gans, U. S. Schubert, *J. Mater. Chem.* **2004**, 14, 2627.
- [14] B.-J. de Gans, P. C. Duineveld, U. S. Schubert, *Adv. Mater.* **2004**, 16, 203.
- [15] *Inkjet Technology for Digital Fabrication* (Eds: I. M. Hutchings, G. D. Martin), Wiley, Chichester **2013**.
- [16] T. M. Eggenhuisen, Y. Galagan, A. Biezemans, M. Coenen, J. Gilot, P. Groen, R. Andriessen, *40th Photovoltaic Specialist Conf. IEEE*, Denver, CO **2014**, pp. 2842–2845.
- [17] S. Ganesan, S. R. Gollu, J. Alam Khan, A. Kushwaha, D. Gupta, *Opt. Mater.* **2019**, 94, 430.
- [18] P. Maisch, K. C. Tam, L. Lucera, H.-J. Egelhaaf, H. Scheiber, E. Maier, C. J. Brabec, *Org. Electron.* **2016**, 38, 139.
- [19] S. Kommeren, M. J. J. Coenen, T. M. Eggenhuisen, Thijs M. W. L. Slaats, H. Gorter, P. Groen, *Org. Electron.* **2018**, 61, 282.
- [20] C. McDowell, G. C. Bazan, *Curr. Opin. Green Sustain. Chem.* **2017**, 5, 49.
- [21] C. A. Lamont, T. M. Eggenhuisen, M. J. J. Coenen, T. W. L. Slaats, R. Andriessen, P. Groen, *Org. Electron.* **2015**, 17, 107.
- [22] D. Corzo, K. Almasabi, E. Bihar, S. Macphée, D. Rosas-Villalva, N. Gasparini, S. Inal, D. Baran, *Adv. Mater. Technol.* **2019**, 4, 1900040.
- [23] E. Bihar, D. Corzo, T. C. Hidalgo, D. Rosas-Villalva, K. N. Salama, S. Inal, D. Baran, *Adv. Mater. Technol.* **2020**, 5, 2000226.
- [24] P. Schilinsky, C. Waldauf, C. J. Brabec, *Adv. Funct. Mater.* **2006**, 16, 1669.
- [25] J. E. Fromm, *IBM J. Res. Dev.* **1984**, 28, 322.
- [26] H. Hu, R. G. Larson, *J. Phys. Chem. B* **2006**, 110, 7090.
- [27] D. Soltman, V. Subramanian, *Langmuir* **2008**, 24, 2224.
- [28] D. Qian, L. Ye, M. Zhang, Y. Liang, L. Li, Y. Huang, X. Guo, S. Zhang, Z. Tan, J. Hou, *Macromolecules* **2012**, 45, 9611.
- [29] Y. Lin, J. Wang, Z.-G. Zhang, H. Bai, Y. Li, D. Zhu, X. Zhan, *Adv. Mater.* **2015**, 27, 1170.
- [30] M. Zhang, X. Guo, W. Ma, H. Ade, J. Hou, *Adv. Mater.* **2015**, 27, 4655.
- [31] W. Zhao, S. Li, H. Yao, S. Zhang, Y. Zhang, B. Yang, J. Hou, *J. Am. Chem. Soc.* **2017**, 139, 7148.
- [32] S. Dong, K. Zhang, T. Jia, W. Zhong, X. Wang, F. Huang, Y. Cao, *EcoMat* **2019**, 1, eom2.12006.
- [33] A. Singh, S. K. Gupta, A. Garg, *Org. Electron.* **2016**, 35, 118.
- [34] J. Park, J. Moon, *Langmuir* **2006**, 22, 3506.
- [35] N. Reis, B. Derby, *MRS Proc.* **2000**, 625, 117.
- [36] Y. Cui, H. Yao, L. Hong, T. Zhang, Y. Tang, B. Lin, K. Xian, B. Gao, C. An, P. Bi, W. Ma, J. Hou, *Natl. Sci. Rev.* **2020**, 7, 1239.
- [37] D. Corzo, E. Bihar, E. B. Alexandre, D. Rosas-Villalva, D. Baran, *Adv. Funct. Mater.* **2020**, 31, 2005763.
- [38] T. Kirchartz, J. Nelson, *Phys. Rev. B* **2012**, 86, 165201.
- [39] A. Guerrero, S. Loser, G. Garcia-Belmonte, C. J. Bruns, J. Smith, H. Miyachi, S. I. Stupp, J. Bisquert, T. J. Marks, *Phys. Chem. Chem. Phys.* **2013**, 15, 16456.
- [40] G. Garcia-Belmonte, A. Guerrero, J. Bisquert, *J. Phys. Chem. Lett.* **2013**, 4, 877.
- [41] A. Guerrero, H. Heidari, T. S. Ripolles, A. Kovalenko, M. Pfannmöller, S. Bals, L.-D. Kauffmann, J. Bisquert, G. Garcia-Belmonte, *Adv. Energy Mater.* **2015**, 5, 1401997.
- [42] K. A. Luck, V. K. Sangwan, P. E. Hartnett, H. N. Arnold, M. R. Wasielewski, T. J. Marks, M. C. Hersam, *Adv. Funct. Mater.* **2017**, 27, 1703805.
- [43] T. Ripolles-Sanchis, A. Guerrero, J. Bisquert, G. Garcia-Belmonte, *J. Phys. Chem. C* **2012**, 116, 16925.
- [44] G. Garcia-Belmonte, A. Munar, E. M. Barea, J. Bisquert, I. Ugarte, R. Pacios, *Org. Electron.* **2008**, 9, 847.
- [45] A. L. Patterson, *Phys. Rev.* **1939**, 56, 978.
- [46] S.-J. Ko, W. Lee, H. Choi, B. Walker, S. Yum, S. Kim, T. J. Shin, H. Y. Woo, J. Y. Kim, *Adv. Energy Mater.* **2015**, 5, 1401687.
- [47] W. Köntges, P. Perkhun, J. Kammerer, R. Alkarsifi, U. Würfel, O. Margeat, C. Videlot-Ackermann, J.-J. Simon, R. R. Schröder, J. Ackermann, M. Pfannmöller, *Energy Environ. Sci.* **2020**, 13, 1259.
- [48] S. Dong, K. Zhang, T. Jia, W. Zhong, X. Wang, F. Huang, Y. Cao, *EcoMat* **2019**, e12006.
- [49] L. Zhang, H. Zhao, B. Lin, J. Yuan, X. Xu, J. Wu, K. Zhou, X. Guo, M. Zhang, W. Ma, *J. Mater. Chem. A* **2019**, 7, 22265.
- [50] S. B. Dkhil, M. Pfannmöller, M. I. Saba, M. Gaceur, H. Heidari, C. Videlot-Ackermann, O. Margeat, A. Guerrero, J. Bisquert, G. Garcia-Belmonte, A. Mattoni, S. Bals, J. Ackermann, *Adv. Energy Mater.* **2017**, 7, 1601486.
- [51] A. B. D. Cassie, *Discuss. Faraday Soc.* **1948**, 3, 11.
- [52] F. Bencheikh, D. Duché, C. M. Ruiz, J.-J. Simon, L. Escoubas, *J. Phys. Chem. C* **2015**, 119, 24643.
- [53] R. F. Egerton, *Electron Energy-Loss Spectroscopy in the Electron Microscope*, Springer US, Boston, MA **2011**.
- [54] F. de la Peña, E. Prestat, V. Tonaas Fauske, P. Burdet, P. Jokubauskas, M. Nord, T. Ostasevicius, K. E. MacArthur, M. Sarahan, D. N. Johnstone, J. Taillon, J. Lähnemann, V. Migunov, A. Eljarrat, J. Caron, T. Aarholt, S. Mazzucco, M. Walls, T. Slater, F. Winkler, B. Martineau, G. Donval, R. McLeod, E. R. Hoglund, I. Alxneit, D. Lundeby, T. Henninen, L. Fernando Zagonel, A. Garmannslunde la Peña, HyperSpy v1.5.2.
- [55] C. Sommer, C. Straehle, U. Kothe, F. A. Hamprecht, *IEEE Int. Symp. on Biomedical Imaging: From Nano to Macro*, IEEE, Chicago, IL **2011**, pp. 230–233.
- [56] M. Pfannmöller, H. Flügge, G. Benner, I. Wacker, C. Sommer, M. Hanselmann, S. Schmale, H. Schmidt, F. A. Hamprecht, T. Rabe, W. Kowalsky, R. R. Schröder, *Nano Lett.* **2011**, 11, 3099.